

Interfacial interaction promoted titanium oxide-based organic-inorganic nanoheterojunctions by chiral host-guest binding

Juexin Huang^{1,2}, Jingyi Xia¹, Sravan Baddi¹ & Chuanliang Feng¹  [✉]

Although titanium oxide (TiO₂)-based organic-inorganic nanostructures attract increasing attention in energy fields, accurate regulation of close contact between TiO₂ and organic components in nanostructures that determines their performance is still a critical task. Here, the interfacial interaction in TiO₂-based organic-inorganic nanoheterojunctions is promoted by host-guest interactions, which are obtained through chiral recognition between chirality imprinted TiO₂ and chiral organic molecules (L-PheAD), leading to their close contact. This close contact is due to the matching structure obtained from a multi-level chirality transfer between TiO₂ and L-PheAD during molecular imprinting, facilitating the strong electronic coupling and resulting in a positive correlation between chiral signal intensity and the interface bonding strength in the nanoheterojunction. The tightly packed interface is further confirmed by the enhanced photocatalytic activity of TiO₂-L-PheAD nanoheterojunctions. This work creates an opportunity to tailor the intimate contact between organic-inorganic interfaces based on host-guest systems with matched chiral space.

¹State Key Lab of Metal Matrix Composites, Shanghai Key Laboratory for Molecular Engineering of Chiral Drugs, School of Materials Science and Engineering, Shanghai Jiao Tong University, 800 Dongchuan Road, Shanghai 200240, P. R. China. ²School of Chemical and Chemical Engineering, Yili Normal University, 448 Jiefang West Road, Yining 835000, P.R. China. ✉email: clfeng@sjtu.edu.cn

The investigation of close contact between TiO₂ and organic components is very important since it highly determines the efficiency of TiO₂-based organic-inorganic nanostructures used for photocatalysts^{1–5}, sensor devices⁶, and energy storage devices^{7,8}. The binding between TiO₂ and organic components is mainly achieved through non-covalent interactions^{9,10} (e.g., electrostatic interactions, hydrophobic interactions, and hydrogen bonding) and/or covalent linkages^{11,12} by the calcination^{13,14}, sol-gel^{15,16}, hydrothermal/solvothermal process^{17,18}, the impregnation method or post-synthetic modification of inorganic nanoparticles^{19,20}. However, non-covalent interactions are weak short-range attractions, which are vulnerable to destruction by mechanical force²¹ or weakened by solvent molecules²². The formation of covalent linkages between TiO₂ and organic components often requires additional coupling agents which are unstable under multiple operating conditions^{23–25}. These always lead to a decrease in the structural stability and functional efficiency of TiO₂-based organic-inorganic hybrid materials due to the separation between TiO₂ and organic components^{26,27}. It is still a great challenge to tightly integrate these two different components together to promote interfacial interaction^{11,28}.

In situ reaction is an effective way to enhance interfacial interaction in organic-inorganic composites. Li and coworkers closely bound TiO₂ and organic covalent organic framework (COF) by covalent bonds through a Schiff base reaction, obtaining a hybrid heterostructure photocatalyst with efficient photocatalytic activity¹¹. An organic-inorganic hybrid system with improved stability of the doped C4BTP dyes was also achieved by the sol-gel method¹². Another effective method is hydrolysis and self-assembly-based multiple-reaction. Yang and coworkers prepared the COF/TiO₂ composites with uniformly embedded TiO₂ nanodots in the interlayers of the porous COF²⁷. Jiang et al. reported a composite containing metal-organic frameworks with TiO₂ in specific pores by the inclusion and gradual hydrolysis of titanium n-butoxide as the TiO₂ precursor⁴. Despite these advances, the formation of covalent bonds between TiO₂ and organic components usually requires the presence of organic linkers, which are highly unstable under operating conditions and can be leached out during application (e.g., photocatalysis)^{12,29,30}. Besides, the hydrolysis process of TiO₂ precursors in these methods often results in phase separation^{31,32}, which may decrease the compatibility between the TiO₂ and organic components³³.

Alternatively, host-guest systems show great potential for achieving intimately and uniformly mixed organic-inorganic substructures due to their highly specific binding affinities^{20,34}. Herein, the promoted interfacial interaction in TiO₂-based organic-inorganic nanoheterojunctions was achieved via host-guest interaction through chiral recognition between TiO₂ and chiral organic molecules. The chiral imprinted TiO₂ was obtained through the successful chirality transfer from template molecules (L-PheAD and D-PheAD, Fig. 1a) to the cross-linked TiO₂ by flexible molecular imprinting technique (MIT) (Fig. 1b, c). The transferred chirality is obtained not only from the asymmetric carbon but also from the L-PheAD side chains (the chirality of achiral -Ph-NH-Ph segment was transferred from phenylalanine group during self-assembly). As L-PheAD side chains (-Ph-NH-Ph group) with large steric hindrance beside the chiral carbon could generate stable conformations, the structure transferred to TiO₂ could be maintained during MIT. When chiral TiO₂ co-assembled with L-PheAD, they bound to these -Ph-NH-Ph groups. These tightly packed structures in nanoheterojunction could facilitate strong electronic coupling, resulting a positive correlation between chiral signal intensity and the interface bonding strength. With more effective bonding between the

imprinted TiO₂ and organic components, the interfacial electrical resistivity continuously decreases and stronger electronic coupling can be obtained, leading to a higher chiral signal. The effective combination of imprinted TiO₂ and L-PheAD can be further proved by the promoted photocatalytic activity of TiO₂-based nanoheterojunction and H₂ generation rate may be up to 2472.5 μmol g⁻¹ h⁻¹, which is 3.3 times higher than the rate of the blank-TiO₂-L-PheAD. This work illuminates the possibility to construct other organic-inorganic hybrid materials with precisely controlled heterojunction structures.

Results

Preparation of chiral molecularly imprinted TiO₂. The chiral molecularly imprinted TiO₂ photocatalysts were synthesized by sol-gel method and titanium tetraisopropanolate was used as the precursor. TiO₂ products tend to aggregate into large agglomerates with a basic catalyst³⁵, which may create an ideal environment for imprinting chiral L-PheAD (Fig. 2a) into sol-gel TiO₂. The formation of chiral spaces in imprinted TiO₂ inorganic nanocrystals can be controlled since chiral molecules have different affinities to the different crystal faces of inorganic nanocrystals^{36,37}. The X-ray diffractometer (XRD) patterns of the crystalline phases of TiO₂ (Supplementary Fig. 1a and Supplementary Table 1) show that the content of anatase phase firstly increases and then decreases with increasing chain length of the added basic catalyst. The highest content of anatase was prepared with adding n-propylamine (denoted as TiO₂-b) and it was selected as the basic catalyst.

To improve the binding efficiency, the concentration of L-PheAD was increased to promote the formation of sufficient footprints on the xerogels³⁸. TiO₂-0, TiO₂-1, TiO₂-2l, and TiO₂-3 were prepared by adding 0, 35, 70, and 140 mg of L-PheAD, respectively. TiO₂-0 and TiO₂-3 contain a lower anatase phase content than the others (Supplementary Fig. 1b and Supplementary Table 2) due to the phase transformation of the anatase during heating. Since the excessive amounts of L-PheAD in TiO₂-3 could induce uneven mixing of L-PheAD and TiO₂ precursors, it led to the localized overheating during heat treatment and in turn the phase transferred from anatase to rutile. The imprinting efficiency of MIT was evaluated by circular dichroism (CD) spectroscopy. The CD signals of TiO₂-2l and TiO₂-2d (with adding 70 mg D-PheAD) display a mirror-image (Supplementary Fig. 1c), demonstrating the successful molecular chirality transfer from L-PheAD/D-PheAD to TiO₂-2l/TiO₂-2d. This suggests that increasing the number of template molecules while maintaining uniform dispersion may help to increase imprinting efficiency.

The effect of L-PheAD concentration was further verified by scanning electron microscopy (SEM). TiO₂-0 has a definite spherical shape, a coexistence of spherical and irregular particles for TiO₂-1, and uniform rod-like morphology for TiO₂-2l (Fig. 2b, c and Supplementary Fig. 2a, b). Typically, the morphology of TiO₂-2l is very similar to that of L-PheAD (Fig. 2d, f), suggesting the influence of L-PheAD on TiO₂ morphology. In addition, the existence of large particles of TiO₂-3 with a lot of micro pores on their surface was observed (Fig. 2e and Supplementary Fig. 2c).

Characterization of inorganic-organic hybrid structures. The co-assembly was investigated to find the best matching system for forming inorganic-organic nanoheterojunctions. Chiral properties of the co-assemblies were studied by CD and anisotropy factor (g-factor) spectra. The equation for calculating g-factor value is given below: $g_{\text{abs}} = \text{CD}(\text{mdeg}) / (32980 \times \text{Abs})$ ³⁹. The g_{abs} value of TiO₂-L-PheAD initially increased and then decreased with increasing TiO₂-2l concentration. When 10 μL of acetonitrile containing TiO₂-2l was added, the g_{abs} reached a maximum of

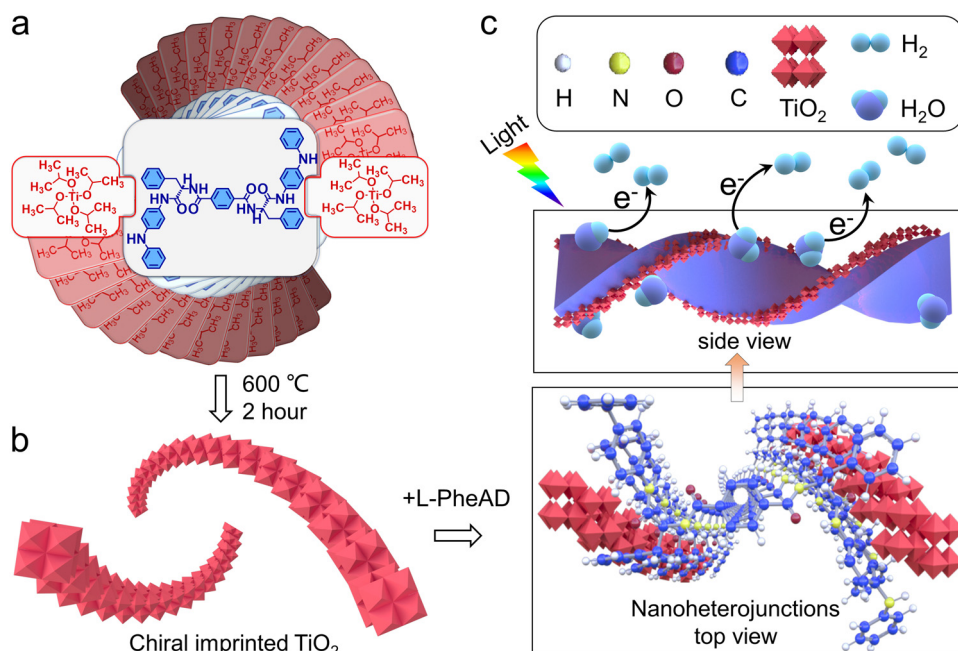


Fig. 1 Schematic illustrations of TiO₂-L-PheAD nanoheterojunctions and the chirality-related hydrogen production capacity. **a** Self-assembly of L-PheAD with TiO₂ precursor; **b** All organic compounds are removed by calcination at 600 °C to prepare chiral imprinted TiO₂; **c** TiO₂-L-PheAD nanoheterojunctions can improve chiral signal and hydrogen production efficiency.

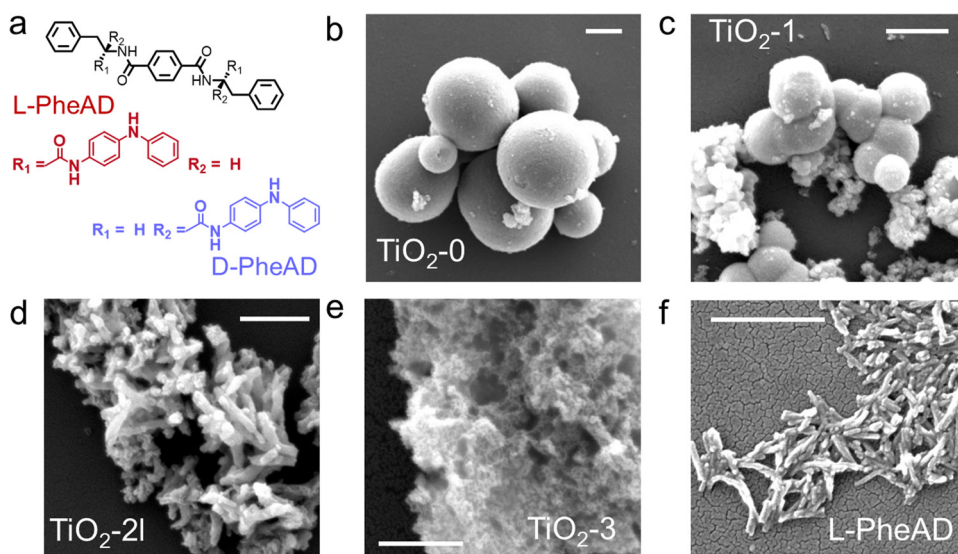


Fig. 2 The morphology of imprinted TiO₂. **a** Chemical structures of the chiral L- or D-phenylalanine-based template molecules (L-PheAD or D-PheAD); **b-f** SEM images of **b** TiO₂-0, **c** TiO₂-1, **d** TiO₂-2l, **e** TiO₂-3, **f** L-PheAD. Scale bars represent: 1 μm.

9.6×10^{-3} (Supplementary Fig. 3a, b). The CD and g-factor spectra for TiO₂-2l-L-PheAD and TiO₂-2l-D-PheAD exhibit different changing trend in the region of 240–300 nm with increasing amounts of TiO₂-2l (Supplementary Fig. 3a). Here, CD spectra of TiO₂-2l-L-PheAD show the strongest CD signals around 250 nm (from amide linkage and benzene ring)⁴⁰ and 276 nm (from N-phenyl-1, 4-phenylenediamine, -Ph-NH-Ph denoted as AD), indicating effective coupling between TiO₂ and L-PheAD, which is correlated with the electronic coupling between relative location and electric dipole transition moments of each chromophore in co-assemblies (Supplementary Figs. 4, 5d, e)^{41,42}. While, the g_{abs} of TiO₂-2l-D-PheAD decreases with increasing amounts of TiO₂-2l (Supplementary Fig. 3b). This suggests a high stereoselectivity between TiO₂-2l and L-/D-

PheAD, and the matching ability of L-PheAD with TiO₂-2l is better than that of D-PheAD. This is further supported by different ultraviolet (UV) spectra of L-PheAD adsorbed on TiO₂-2l and TiO₂-2d (Supplementary Fig. 6b). More L-PheAD can be adsorbed on TiO₂-2l than on TiO₂-2d after 48 h.

An ideal solvent system for the co-assembly of TiO₂ and L-PheAD was further assessed by CD (Supplementary Fig. 7) and g-factor. The co-assembled L-PheAD with TiO₂-1, TiO₂-2l, or TiO₂-3 exhibits similar CD spectral variation patterns in various acetonitrile/water mixtures (Fig. 3a and Supplementary Figs. 8a, 9a, d). In the range of 250–300 nm, the maximum CD signal and g-factor value were obtained in acetonitrile/water (7/3 (v/v)), and the strongest CD signal was obtained for TiO₂-2l-L-PheAD (Fig. 3a and Supplementary Fig. 8a, b). Unsurprisingly, from the

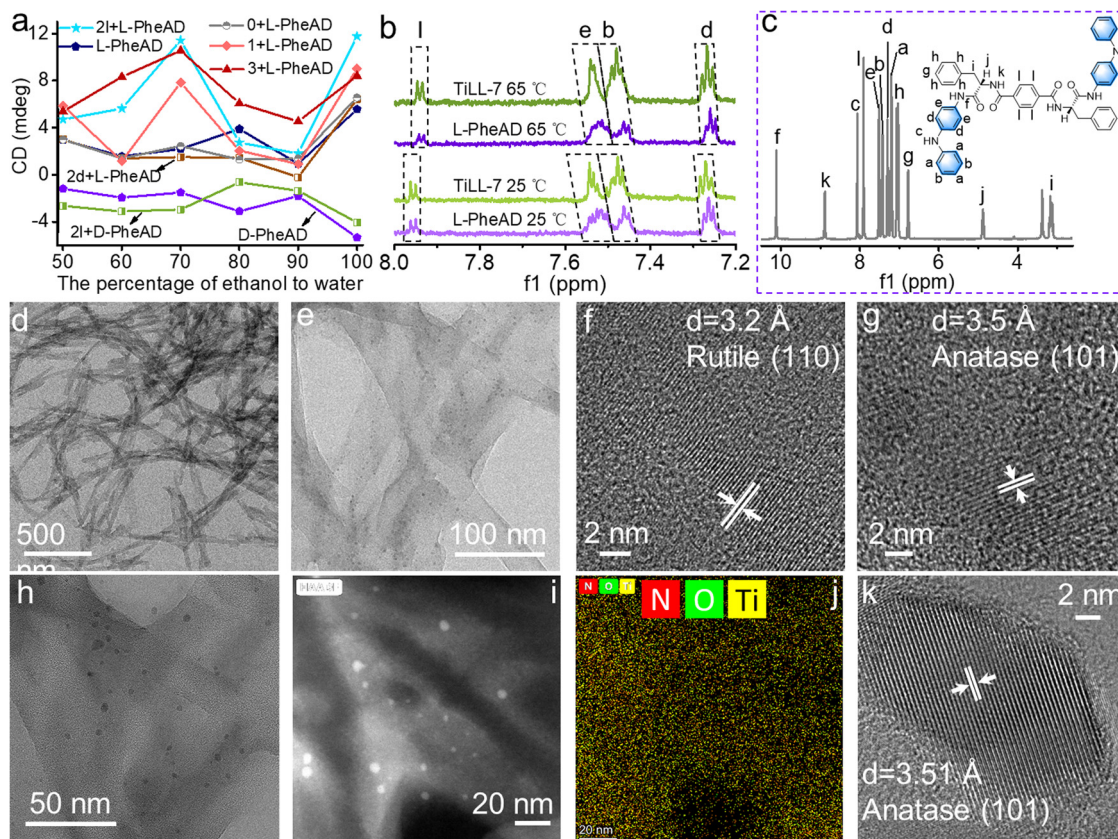


Fig. 3 CD spectroscopy and structural characterization of hybrid materials and TiO₂. **a** Peak values of CD signal in the range of 250–300 nm of TiO₂-L/D-PheAD hybrid materials and L/D-PheAD in mediums composed of water and acetonitrile in various ratios. (2l + L-PheAD, blue line: TiO₂-2l-L-PheAD; 0 + L-PheAD, gray line: TiO₂-0-L-PheAD; 1 + L-PheAD, pink line: TiO₂-1-L-PheAD; 3 + L-PheAD, red line: TiO₂-3-L-PheAD; 2d + L-PheAD, brown line: TiO₂-2d-L-PheAD; 2l + D-PheAD, green line: TiO₂-2l-D-PheAD); **b** ¹H NMR of L-PheAD (purple line) and TiLL-7 (deuterated solvent: deuterated acetonitrile/deuterated water = 7/3); **c** ¹H NMR of L-PheAD in deuterated DMSO-d₆; **d–j** TEM images (**d, e, h**), high-resolution TEM (HRTEM) images (**f, g**), HAADF-scanning transmission electron microscopy (STEM) images (**i**) and corresponding elemental mappings (**j**) for TiLL-7 (TiO₂-2l-L-PheAD formed in acetonitrile/water 7:3 (v/v)); **k** HRTEM image of TiO₂-2l.

appearances of TiO₂-2l-L-PheAD dispersions, TiO₂-2l-L-PheAD can only uniformly dispersed in acetonitrile/water (7/3 (v/v), Supplementary Figs. 10a, b). L-PheAD showed a different variation in CD compared to TiO₂-2l-L-PheAD, and the maximum CD signal in the range of 250–300 nm was obtained in pure acetonitrile, confirming the influence of TiO₂-2l on the assembly behavior of L-PheAD (Fig. 3a and Supplementary Fig. 8d, e). Interestingly, the changes for TiO₂-2d-L-PheAD and TiO₂-0-L-PheAD CD spectra were almost the same as those for L-PheAD, suggesting that the structure of L-PheAD assemblies was not affected by adding TiO₂-2d or TiO₂-0 (Fig. 3a and Supplementary Fig. 11a, b, d, e). A similar phenomenon was observed, when D-PheAD co-assembled with TiO₂-2l (Fig. 3a and Supplementary Fig. 8a, b). These results demonstrate that an efficient host-guest system consisting of TiO₂-2l and L-PheAD can be obtained with matching chiral architectures in acetonitrile/water (7/3 (v/v)).

Temperature-dependent CD and variable-temperature ¹H NMR studies were carried out on TiO₂-2l-L-PheAD and L-PheAD in an acetonitrile/water mixture (7/3 (v/v)) to determine the binding sites in TiO₂-2l-L-PheAD. The results showed that the chiral structure of TiO₂-2l-L-PheAD in acetonitrile/water (7/3) mixture (denoted as TiLL-7) was more stable than that of L-PheAD from 20 to 90 °C (Supplementary Fig. 12). Specifically, the CD peak at ~320 nm assigned to the J-stacked AD segments⁴³ in TiLL-7 maintain the chirality over the temperature range 20–90 °C, while the CD peak at ~320 nm of L-PheAD gradually decreased until complete disappearance

due to the disassociation of J-aggregation. Moreover, TiLL-7 exhibited significant CD signals of AD segments even at 75 °C, while L-PheAD only show chirality at temperatures below 65 °C, from 85 to 25 °C (Supplementary Fig. 13). These CD spectra indicate that the presence of chiral TiO₂ reinforces the chiral structure in J-stacked AD chain segments. The effects of the chiral TiO₂ on the π - π interaction between L-PheAD molecules were further tested by performing liquid phase ¹H NMR experiments. When a nucleus was placed above or below the plane of an aromatic structure, electronic shielding would occur^{44,45}. Therefore, up-field NMR chemical shifts induced by ring current effect can support the π - π stacking geometry of assemblies. At both 25 °C and 65 °C, the same chemical shift of hydrogen atoms (l) in the central benzene ring of TiLL-7 and L-PheAD was observed, while an up-field shift was observed for hydrogen atoms (e, b, d) in AD segments of L-PheAD, as compared to that of TiLL-7 (Fig. 3b, c and Supplementary Fig. 14). This indicates that the electronic shielding effect on the AD segment in the L-PheAD molecule is stronger than that on TiLL-7. J-stacked AD structures exist in both TiLL-7 and L-PheAD at the test temperature and are more stable in TiLL-7 than in L-PheAD, as explored earlier. These findings illustrate that the chiral TiO₂ binding site of L-PheAD in TiLL-7 is AD segments, which decreases the ring current in AD segments, leading to a down-field shift of hydrogen atoms in AD of TiLL-7 compared to L-PheAD.

Scanning electron microscopy energy dispersive spectrometry (SEM-EDS) was used to investigate the morphology and elements

of L-PheAD and TiO₂-L-PheAD. All TiO₂-2l-L-PheAD samples maintained the fibrous structure with various acetonitrile/water mixtures (Supplementary Figs. 15–20). The Ti content in TiO₂-2l-L-PheAD reaches its maximum value when the ratio of acetonitrile/water is 7/3 (Supplementary Fig. 18). However, the distribution of Ti in TiO₂-2d-L-PheAD is uneven due to the unsuccessful co-assembly between TiO₂-2d and L-PheAD (denoted as TiLL-7; Supplementary Fig. 19), which is consistent with CD spectra (Fig. 3a and Supplementary Fig. 11a, b).

Transmission electron microscopy (TEM) was used to evaluate the morphological characteristics and the crystallography information of TiLL-7. TiLL-7 nanofibers are ~50 nm in diameter and interlace with each other (Fig. 3d, e). TiO₂-2l nanoparticles were embedded in a dispersed manner within the L-PheAD nanofibers. The interplanar spacing of the crystal lattice is ~0.35 nm, which matches well with the (101) plane of anatase TiO₂⁴⁶. And the latticing fringe of ~0.25 nm is corresponding to the (101) plane of rutile TiO₂⁴⁷ (Fig. 3f, g and Supplementary Figs. 21, 22). In the high-angle annular dark field (HAADF) image, the bright spot clearly illustrates the distribution of Ti element (Fig. 3i). The TiLL-7 nanofibers can be further identified under EDS element mapping (Fig. 3j and Supplementary Fig. 23). Ti, N, and O are uniformly distributed through the entire fiber, indicating that hybrid nanocomposites have been successfully obtained through co-assembly.

The host-guest interactions between TiO₂-2l and L-PheAD were recorded by XRD patterns (Fig. 4a and Supplementary Fig. 24). Both characteristic peaks possessed by L-PheAD and TiO₂-2l are observed in TiO₂-2l-L-PheAD. When the acetonitrile/water ratio is between 8/2 and 5/5, the peak at ~20° from the π -stacked aromatics⁴⁸ of L-PheAD and the peak at ~25.5° assigned characteristic peak of (101) plane in anatase TiO₂ were observed to move to higher degrees, indicating their closer intermolecular distances than those of other TiO₂-2l-L-PheAD co-assemblies. It was speculated that the squeezing effects of L-PheAD molecules

on TiO₂-2l could change the (101) d-spacing in TiO₂-2l. This interaction can be further validated by dynamic light scattering (DLS) data (Fig. 4b). The TiO₂-2l and L-PheAD show the peaks around 124 nm and 1284 nm, respectively. While TiLL-7 shows a complex peak in the 350–820 nm region, accompanied by a decrease in the DLS signal intensity of the original TiO₂-2l peak at 124 nm and a disappearance of the original L-PheAD peak at 1284 nm (Fig. 4b). These optical signatures are the result of the co-assembly between TiO₂-2l and L-PheAD. In addition, the structure of these TiO₂-2l-L-PheAD nanostructures is very stable and can withstand mechanical forces produced by ultrasound (Supplementary Figs. 25, 26).

Fourier transform infrared spectroscopy (FTIR) measurements provide valuable information about the molecular-level interaction within the co-assemblies (Fig. 4c, d and Supplementary Fig. 27). The as-prepared TiO₂-2l-L-PheAD exhibits two absorption bands in the range of 3357–3289 cm⁻¹ (stretching vibrations (ν NH) of N–H bonds in amide-amide hydrogen bonds (C=O–H–N))⁴⁹ and of 1620–1573 cm⁻¹ (coupled N–H in-plane bending in peptide bond (δ NH))⁵⁰. The shape and position of these absorption bands in TiO₂-2l-L-PheAD are consistent with L-PheAD, indicating intermolecular hydrogen bonding between L-PheAD is partially retained. TiLL-7 has the lowest peak intensity among TiO₂-2l-L-PheAD hybrid nanostructures due to insertion of the largest amount of TiO₂ nanoparticles in L-PheAD, which can block the interaction (hydrogen bonds) between L-PheAD molecules. By thermogravimetry (TG) and its derivative (DTG), the effects of TiO₂-2l insertion into L-PheAD on thermal durability were investigated. The thermal stability was increased with adding TiO₂-2l to L-PheAD and the best thermal stability was obtained by TiLL-7 among the other TiO₂-2l-L-PheAD co-assemblies (Fig. 4e and Supplementary Fig. 28).

The changes in the surface composition of TiO₂-2l-L-PheAD can be observed through water contact angle and Scanning Kelvin probe microscopy (SKPM). The most hydrophilic surface for

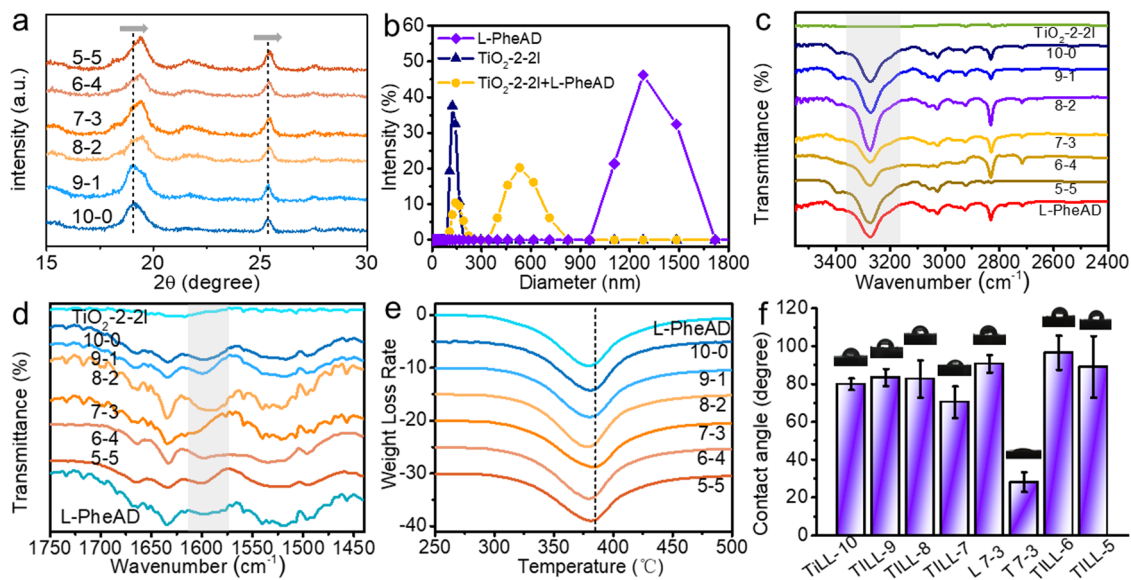


Fig. 4 The interaction between TiO₂ and L-PheAD. **a** Powder X-ray diffraction pattern of TiO₂-L-PheAD formed in mediums composed of water and acetonitrile in various ratios (5–5, red line: acetonitrile/water = 5/5; 6–4, light red line: acetonitrile/water = 6/4; 7–3, purple line: acetonitrile/water = 7/3; 8–2, light purple line: acetonitrile/water = 8/2; 9–1, brown line: acetonitrile/water = 9/1; 10–0, yellow line: acetonitrile/water = 10/0); **b** DLS spectra of TiO₂-2l (dark blue line), L-PheAD (purple line) and TiLL-7 (yellow line); **c, d** Fourier transform infrared spectroscopy of TiO₂-2l, L-PheAD, and TiO₂-2l-L-PheAD; **e** DTG curves of L-PheAD and TiO₂-2l-L-PheAD; **f** water contact angle of TiO₂-2l, L-PheAD, and TiO₂-2l-L-PheAD. L 7–3: L-PheAD obtained from a mixture of acetonitrile and water (7/3, v/v); T 7–3: TiO₂-2l obtained from a mixture of acetonitrile and water (7/3, v/v); TiLL-10, TiLL-9, TiLL-8, TiLL-7, TiLL-6, TiLL-5: TiO₂-2l-L-PheAD obtained from the mixture of acetonitrile and water of 10/0, 9/1, 8/2, 7/3, 6/4, and 5/5 (v/v), respectively. Error bars represent the standard deviations from the statistic results of five sets of experiments.

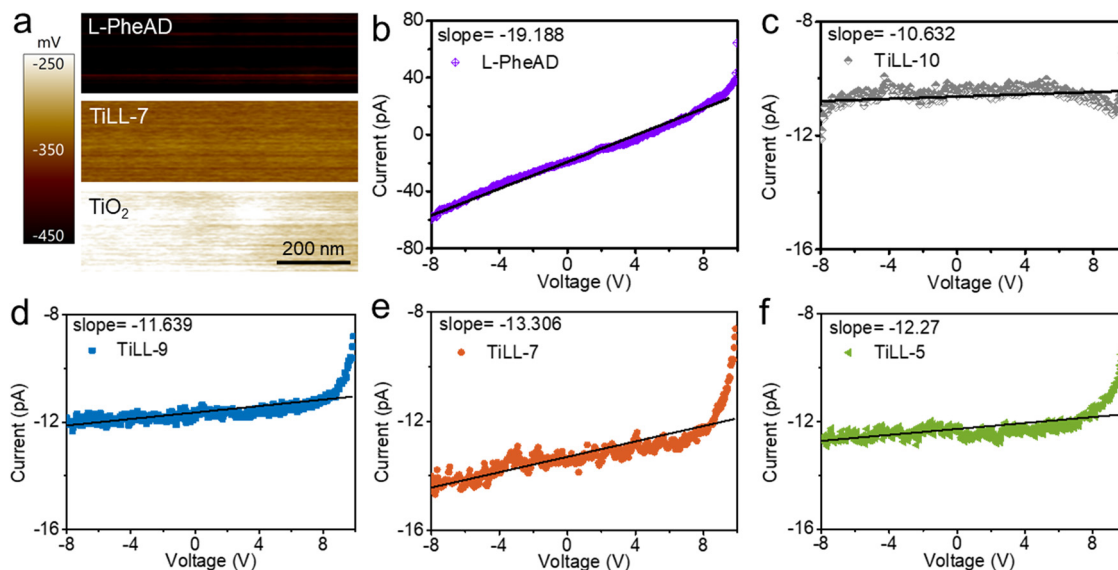


Fig. 5 The electrical properties of L-PheAD and TiO₂-2l-L-PheAD hybrid nanofibers. **a** Surface potential of L-PheAD, TiLL-7, and TiO₂-2l; Typical I-V curves obtained for **b** L-PheAD nanofibers, **c** TiLL-10, **d** TiLL-9, **e** TiLL-7, and **f** TiLL-5.

TiLL-7 among the TiO₂-2l-L-PheAD samples was proved by water contact angle (Fig. 4f). Meanwhile, derived from the SKPM data, the surface potential value of TiLL-7 is between that of TiO₂-2l and L-PheAD (Fig. 5a and Supplementary Fig. 29). The electrical properties of L-PheAD and TiO₂-2l-L-PheAD hybrid nanofibers were measured by conductive atomic force microscopy (CAFM). The electrical resistivity of L-PheAD nanofibers calculated from I-V curves is $\sim 9.51 \times 10^3 \Omega\text{-cm}$ (Fig. 5b and Supplementary Fig. 30). The resistivity of the hybrid nanofibers increased with adding TiO₂-2l (Fig. 5b–f). Meanwhile, the electrical resistivity value of TiLL-7 is the smallest among the co-assemblies (Fig. 5e and Supplementary Fig. 31), which reflects the lowest interfacial contact resistance and indicates effective interfacial interactions⁵¹. The resistivity values of the samples follow the order of TiLL-9 > TiLL-5 > TiLL-10 > TiLL-7 (Supplementary Fig. 31), and the magnitude of their CD signal follow the order of TiLL-7 > TiLL-10 > TiLL-5 > TiLL-9 (Fig. 3a), showing a positive correlation between chiral signal intensity and the interface bonding strength in nanoheterojunctions.

Photophysical, electrochemical properties, and photocatalysis activity of co-assemblies. The electrochemical band gaps of TiO₂-2l and L-PheAD were calculated from the difference of oxidation and reduction potentials measured by CV experiments. The HOMO and LUMO energy levels of L-PheAD are higher than those of TiO₂-2l (Supplementary Fig. 32), facilitating the formation of type-II heterojunction between TiO₂-2l and L-PheAD to enhance the photoinduced charges separation efficiency and the photocatalytic performance. The type-II heterojunction structure of TiO₂-2l-L-PheAD was further prove by ultraviolet photoelectron spectroscopy (UPS) and Tauc plots (Supplementary Table 3, Supplementary Fig. 33 and Fig. 6c). The linear sweep voltammetry (LSV) curves of photoelectrodes under visible light irradiation show that TiLL-7 has the highest current density among all samples, and photocurrents of the samples follow the order of TiLL-7 > TiLL-6 \geq TiLL-10 > TiLL-8 \geq TiLL-5 > L-PheAD > TiO₂-2l > TiLL-9 (Fig. 6a and Supplementary Fig. 35c, d). TiLL-7 still has the largest photocurrent density among the others in transient photocurrent responses results, which is consistent with the LSV results (Supplementary Fig. 34). The photocurrents of all TiO₂-2l-L-PheAD hybrid materials

(except for TiLL-9) were much larger than those of TiO₂ or L-PheAD, verifying the synergistic effect of TiO₂-2l and L-PheAD in promoting photocurrent (Supplementary Figs. 34, 35). These improved photocurrents for TiO₂-2l-L-PheAD samples under visible light irradiation indicated that the effective combination of L-PheAD with TiO₂ can improve the efficiency of visible-light utilization of TiO₂.

Electrochemical impedance spectroscopy (EIS) results are studied to unlock the interfacial charge transport resistance between TiO₂-2l-L-PheAD photoanode and electrolyte. In the Nyquist plots of EIS results (Fig. 6b and Supplementary Fig. 36), the semicircle arc radius in the middle frequency range represents the charge transfer properties from the photoanode to the electrolyte⁵². TiLL-7 shows the lowest charge transfer resistance compared to other TiO₂-L-PheAD photoelectrodes, implying that the electrons accumulated on the surface of TiLL-7 can be efficiently transferred to protons or electron acceptors.

By Mott-Schottky (M-S) analysis, linear relationships of $1/C^2$ vs V in the range of -0.6 – 0.8 V with positive slopes suggest n-type semiconductors for all samples (Supplementary Fig. 37). The smallest slope for TiLL-7 ascribes to its highest charge carrier density among TiO₂-2l-L-PheAD hybrid materials⁵³, which agrees with the EIS results. According to flat band potential (V_{fb}) computed by the X-axis intercept of $1/C^2$ vs V , the V_{fb} of TiLL-7 is -0.4 V, this value is between TiO₂-2l (-0.34 V) and L-PheAD (-0.43 V). This is consistent with the findings of CV experiment, which located the HOMO/LUMO position of TiO₂-2l-L-PheAD between TiO₂-2l and L-PheAD (Supplementary Fig. 32). After hybridization between L-PheAD and TiO₂, the typical absorption band of co-assemblies (TiLL-7) was significantly expanded to 200–800 nm (Supplementary Fig. 38). This expansion could be attributed to the successful construction of the TiO₂-2l-L-PheAD heterojunction. TiLL-7 has two distinct band gaps in the Tauc plots: a narrow band gap of 0.84 eV and a wide band gap of 2.88 eV (Fig. 6c). We deduced that the former could be ascribed to L-PheAD and the latter could be attributed to TiO₂-2l.

The effective combination of TiO₂-2l-L-PheAD can be further proved by the promoted photocatalytic activity in hydrogen generation. The H₂ production rate of TiLL-7 hybrid material is $2472.5 \mu\text{mol g}^{-1} \text{h}^{-1}$, which is 2.9 and 6.8 times higher than that of TiO₂-2l and L-PheAD (Fig. 6d). The amount of hydrogen

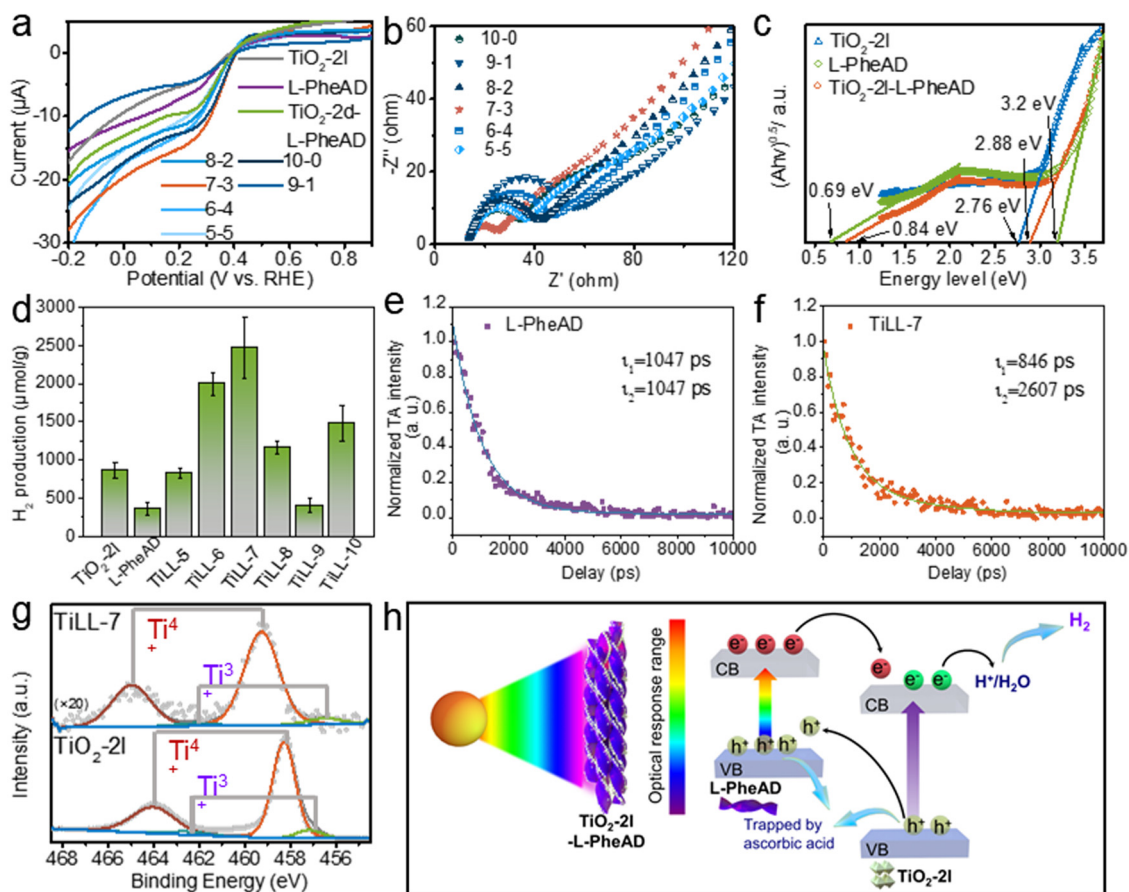


Fig. 6 Photocatalytic performance of $\text{TiO}_2\text{-2l-L-PheAD}$. **a** Liner sweep voltammetry (LSV) curves of $\text{TiO}_2\text{-2l}$, L-PheAD, and $\text{TiO}_2\text{-2l/TiO}_2\text{-2d-L-PheAD}$ (photoelectrodes) under visible light irradiation; **b** Electrochemical impedance spectroscopy (EIS) plots of $\text{TiO}_2\text{-2l-L-PheAD}$ in mediums composed of water and acetonitrile in various ratios; **c** Tauc plot of $\text{TiO}_2\text{-2l}$, L-PheAD, and TiLL-7. **d** Photocatalytic hydrogen production over different samples under simulated sunlight. Error bars represent the standard deviations from the statistic results of three sets of experiments. **e, f** Time-resolved transient PL decay of L-PheAD (**e**) and TiLL-7 (**f**); **g** high-resolution Ti 2p XPS spectra. **h** Schematic illustration of the electron transfer pathways for hydrogen production over $\text{TiO}_2\text{-2l-L-PheAD}$.

production of the samples follows in the order of TiLL-7 > TiLL-6 > TiLL-10 > TiLL-8 > TiLL-5 > TiLL-9, which is almost in agreement with the LSV and transient photocurrent responses ($I-t$) results. A comparison between the hydrogen production efficiency of our experiment and other TiO_2 -based organic-inorganic hybrid materials has been listed in Supplementary Table 4. The photocatalytic hydrogen evolution performance of TiLL-7 is comparable or superior to the reported typical TiO_2 -based organic-inorganic photocatalysts (without metal cocatalysts). Supplementary Fig. 39 shows the results of incident photon-to-current conversion efficiency (IPCE) calculated based on the photocurrent density obtained with 365 nm irradiation. TiLL-7 possessed 4.3 times and 21.5 times higher IPCE values compared to $\text{TiO}_2\text{-2l}$ and L-PheAD, respectively. We have also calculated the apparent quantum efficiency (AQE). AQE as a function of the incident light wavelength (365, 420, and 600 nm) is presented in Supplementary Table 5, indicating a consistent trend with the UV-Vis spectra. The enhanced hydrogen production capacity of $\text{TiO}_2\text{-2l-L-PheAD}$ hybrid material was attributed to the effective self-assembly between imprinted TiO_2 and chiral L-PheAD, leading to intimate contact at their interfaces. However, when blank $\text{TiO}_2\text{-0}$ was co-assembled with L-PheAD, the efficiency of hydrogen production could not be effectively improved, as its H_2 generation rate was $741 \mu\text{mol g}^{-1} \text{h}^{-1}$ (Supplementary Fig. 40). The promotion of hydrogen

production by chiral host-guest interactions in the $\text{TiO}_2\text{-L-PheAD}$ system was compared with by other non-covalent interactions. $\text{TiO}_2\text{-2l}$ and $\text{TiO}_2\text{-0}$ were modified with carboxylic functional groups (Supplementary Figs. 41, 42). Subsequently, the modified $\text{TiO}_2\text{-2l}$ (denoted as $\text{TiO}_2\text{-2l-COOH}$) and $\text{TiO}_2\text{-0}$ (denoted as $\text{TiO}_2\text{-0-COOH}$) were co-assembled with L-PheAD (Supplementary Fig. 43) in a solvent mixture of acetonitrile-water (7:3). Unsurprisingly, both $\text{TiO}_2\text{-2l-COOH}$ and $\text{TiO}_2\text{-0-COOH}$ exhibited increased efficiency of hydrogen evolution when co-assembled with L-PheAD than $\text{TiO}_2\text{-2l-L-PheAD}$ and $\text{TiO}_2\text{-0-L-PheAD}$ (Supplementary Fig. 44). However, the hydrogen generation of $\text{TiO}_2\text{-0-COOH-L-PheAD}$ was significantly lower than that of $\text{TiO}_2\text{-2l-L-PheAD}$, demonstrating that chiral host-guest interactions were more favorable for the promotion of hydrogen production compared to the ionic bond interactions in $\text{TiO}_2\text{-L-PheAD}$ system.

The stability of the $\text{TiO}_2\text{-2l-L-PheAD}$ catalyst system was further studied. Both L-PheAD and $\text{TiO}_2\text{-2l-L-PheAD}$ (TiLL-7) showed the relatively stable photocurrent values at an applied potential of -0.65 V SCE under the UV radiation (365 nm) for two hours (Supplementary Fig. 45). Subsequently, the collected catalyst was characterized by FT-IR, UV-vis and $^1\text{H NMR}$ measurements to detect the stability of the sample after the photocatalytic reactions under UV radiation. As shown in Supplementary Fig. 46 the FT-IR, UV-vis and $^1\text{H NMR}$ spectra

(Supplementary Fig. 47) of the sample before and after the catalytic reactions were similar, and the characteristic peaks showed no obvious change, indicating that the structure of the catalyst was stable before and after reaction under UV radiation. Finally, the stability of TiLL-7 was tested in photocatalytic hydrogen production. As seen from Supplementary Fig. 48, the TiLL-7 catalyst could be dried and recycled at least 3 times to produce hydrogen via photocatalysis under the same conditions (exposed to UV light or simulated sunlight for 1 h).

We further evaluated the photocatalytic activity of TiLL-7 for pollutant degradation under simulated solar light irradiation. Spectroscopic analysis reveals that the photodegradation process causes a significant decrease in the absorption bands of rhodamine B (RhB) and methyl viologen (MV) with time (Supplementary Figs. 49, 50). As expected, TiLL-7 exhibited the highest photodegradation rates, as deduced by first-order rate constants (k) (Supplementary Figs. 49b, 50b). Specifically, during the degradation of 0.45 mM RhB, the k value for TiLL-7 was 1.69-fold and 1.92-fold higher than that of TiO_2 and L-PheAD, respectively. These results indicated that the 5 mg fabricated catalyst (TiLL-7) could degrade ~60% of 215.5 mg L^{-1} RhB (10 ml) in 90 min.

The charge transfer at the combined interface within TiLL-7 was employed by X-ray photoelectron spectroscopy (XPS). In the Ti 2p XPS spectra (Fig. 6g), the bare TiO_2 -2l sample shows two binding energy (BE) peaks at ~464.1 eV and ~458.3 eV, assigned to Ti^{4+} of 2p 3/2 and 2p 1/2, respectively⁵⁴. The shoulder peaks at ~462.2 eV and 456.8 eV indicate the presence of Ti^{3+} in pristine TiO_2 -2l as well as TiLL-7 (Fig. 6g). The Ti^{4+} peaks in TiLL-7 were shifted by ~0.9 eV to a higher BE compared to those of bare TiO_2 -2l. This shift can be attributed to the higher oxidation state of the core metal atom (Ti) induced by nitrogen in the coordination sphere. The N 1s region for L-PheAD is at 399.9 eV, while a negative shift by ~0.1 eV is observed for TiLL-7 (Supplementary Fig. 51a), indicating an increased electron density on N cation⁵⁵, which proves the existence of charge transfer between TiO_2 -2l and L-PheAD. In addition, the shifts in both Ti 2p and N 1s peaks indicate the effective interfacial contacts between TiO_2 -2l units and L-PheAD. It is noteworthy that the atomic ratio of TiLL-7 on the surface for Ti/(Ti + C + N + O) and Ti/N was estimated to be 0.24% and 3%, respectively (estimated by XPS, Supplementary Table 6). However, the overall Ti/(Ti + C + N + O) and Ti/N atomic ratio is 1.6% and 25%, respectively (TiO_2 -2l/L-PheAD=1/1 in TiLL-7), which is higher than the surface concentration and approximately equal to the bulk concentration of Ti atomic in TiLL-7 (Ti/N = 30.8%, Supplementary Fig. 18). This observation suggests that TiO_2 -2l is distributed on both surface and inside of TiLL-7, rather than forming aggregates on the surface of TiLL-7.

The charge transfer within TiO_2 -2l-L-PheAD was investigated by steady-state photoluminescence (PL) spectra and Time-resolved photoluminescence spectra. PL spectra under excitation at 295 and 320 nm show that the L-PheAD and all composites give a broad band from 325 to 410 nm, whereas all composites have lower intensities than L-PheAD (Supplementary Fig. 52). In particular, TiLL-6, TiLL-7, and TiLL-8 produced a larger decrease in fluorescence compared to the others. The reduced PL intensity in the composites reference to the L-PheAD reveals rapid electron transfer from the L-PheAD to TiO_2 -2l⁵⁶, and more efficient electron transfers take place in the TiLL-6, TiLL-7, and TiLL-8 compared to others. Compared with the fluorescence peaks of L-PheAD, the maximum fluorescence peaks of TiLL-6, TiLL-7, and TiLL-8 have a large red shift (Supplementary Fig. 52b), indicating a shrinking of HOMO-LUMO gap^{57,58}. The lifetime of the photogenerated charge carriers for pure L-PheAD and TiLL-7 (PL decay spectroscopy, Fig. 6e, f) can be well fitted by a biexponential

function:

$$I(t) = A_1 e^{-\frac{t}{\tau_1}} + A_2 e^{-\frac{t}{\tau_2}}$$

where A_1 and A_2 represent the corresponding amplitudes of the two components at $t = 0$. Consequently, τ_1 of the L-PheAD and TiLL-7 composite are 1047 ps and 846 ps, respectively. While τ_2 of the L-PheAD and TiLL-7 composite are 1047 Ps and 2607 Ps, respectively. Typically, the short lifetime (τ_1) is induced by quasi-free excitons, which may originate from the recombination of the delocalized carriers in the internal states, while the long lifetime (τ_2) is attributed to the recombination of the localized carriers at the surface^{59,60}. However, as τ_1 and τ_2 for L-PheAD are equal, it indicates that the emission has a nearly single-exponential decay, which suggests high crystallinity and a weak contribution of defects in the electron/hole recombination process⁶¹. Because TiO_2 -2l is distributed on both surface and inside of the TiLL-7, the τ_1 of TiLL-7 is slightly decreased compared to that of L-PheAD, probably because the internal crystalline structure of TiLL-7 appears to have more defects (due to the TiO_2 -2l insertion in L-PheAD) than L-PheAD. The τ_2 of TiLL-7 is much larger than that of L-PheAD because the type II energy level distribution of TiLL-7 (Supplementary Fig. 32) can reduce the probability of electron-hole recombination, resulting in a longer charge carrier lifetime.

Photocatalytic hydrogen production mechanism. A tentative reaction mechanism for photocatalytic hydrogen evolution over hybrid organic-inorganic TiLL-7 has been proposed (Fig. 6h). Firstly, TiO_2 -2l with an imprinted conformation inserts into the L-PheAD molecules is uniformly distributed in co-assemblies, increasing the hydrophilic property and benefiting water splitting. Secondly, this assembled structure enables broadband light absorption of TiO_2 . Under UV light, both TiO_2 -2l and L-PheAD can excite electrons from their valence band (VB) to the conduction band (CB), while under visible light, only L-PheAD can produce photogenerated electrons and holes. These photogenerated electrons and holes flow to the conduction band of TiO_2 -2l and the valence band of L-PheAD, respectively, due to the type-II heterojunction between TiO_2 -2l and L-PheAD. Finally, the electrons in TiO_2 have a large driving force for hydrogen production, and the holes in the TiLL-7 system are consumed by the ascorbic acid. The co-assembled structure of TiLL-7 can effectively increase the harvest of light energy and suppress charge annihilation.

Discussion

To address the weak binding between TiO_2 and organic materials, we have developed a host-guest system prepared by an easy and flexible chiral MIT with imprinted TiO_2 as guest and the chiral template molecule L-PheAD as host. The well-defined chiral structure of TiO_2 was transferred from the L-PheAD, ensuring intimate contact between their organic-inorganic interfaces by Lego-like assembly *via* chiral recognition ability and hydrophobic forces. Since the position of HOMO and LUMO of L-PheAD is higher than that of TiO_2 , a type-II heterojunction formed. The L-PheAD/ TiO_2 heterojunction interface can accelerate the photogenerated electron transfer from L-PheAD to TiO_2 , leading to improved photoactivity. Notably, the photocatalytic hydrogen production performance increases with the enhancing chiral signals of TiO_2 -L-PheAD hybrid materials, reflecting the positive correlation between the effective combination (electronic coupling) of TiO_2 -L-PheAD and their CD signal intensities.

In this study, a chiral host-guest system was obtained from a multi-level chirality transfer between TiO_2 and L-PheAD during molecular imprinting. The tightly integrated organic-inorganic

interfaces resulting from self-assembly processes between TiO₂ and L-PheAD rely on non-covalent bonding interactions under thermodynamic and kinetic control. The matching nano-scale size and chirality between imprinted TiO₂ and L-PheAD create a more favorable enthalpy (from intermolecular interactions). The chiral TiO₂ binding to the AD segments with large steric hindrances can limit the rate of phase separation, leading to the enhancement of the kinetic stability of TiO₂-L-PheAD. This host-guest system differs from macrocyclic-based host-guest systems, possessing great flexibility. The study expands the scope of organic molecules those can be employed for host-guest systems, providing an approach for enhancing organic-inorganic interfacial interactions without relying on electrostatic forces, hydrogen bonding, or covalent linkage. Notably, this strategy readily allows for the construction of organic-inorganic heterostructures through solution self-assembly methods and is conducive to large-scale applications. This work provides an intriguing example of interface engineering between organics and inorganics based on matched nano-space to design model systems for fundamental studies and improves the physicochemical properties of organics-inorganics composites, advancing their applications in photocatalysis, photovoltaics, electrocatalysis, and electron device.

Methods

Preparation of chiral imprinted TiO₂. Our synthesis of template molecules, L-PheAD and D-PheAD, involved a series of steps⁴³:

N-(tert-butoxycarbonyl)-L-phenylalanine (5.31 g, 20.00 mmol) and HOBt (3.51 g, 26 mmol) were combined with N-phenyl-1,4-phenylenediamine (3.68 g, 20 mmol) and DIEA (86 mmol) in dry DCM. After stirring the reaction mixture under an ice-water bath for 0.5 h, EDC-HCl (40 mmol) in dry DCM was added drop-by-drop. Subsequently, all solvents were evaporated with rotatory evaporator, and the resulting residues were dissolved in ethyl acetate. Following recrystallization, the undissolved substance was collected and dried, yielding dark purple crystals (Boc-L-PheAD 7.44 g, 86.1%). Further, Boc-L-PheAD (6.94 g, 17.2 mmol) was processed with trifluoroacetic acid (23 mL) in DCM (40 mL) for 2 h. These residues obtained after solvents evaporation process is dried at 50 °C in the vacuum oven. Then we combined residues, triethylamine (17.0 mL) in DCM (60 mL) with 1,4-benzenedichloride (1.75 g, 8.6 mmol) in batches and stirred at room temperature for 12 h, leading to the formation of a gel-like precipitate. This gel phase was filtered, washed with deionized water, and finally vacuum dried to provide L-PheAD (5.9 g, 7.43 mmol, 92.9%). Similarly, D-PheAD was obtained as a white solid (5.4 g, 85.1%). Detailed NMR spectra of L/D-PheAD can be found in Supplementary Figs. 53–56.

Chiral imprinted TiO₂ nanoparticles can be synthesized over a range of molar compositions of L/D-PheAD:TIP:basic catalyst:n-propanol = x:7:0.4:400, where x can be adjusted in the range of 0.5–2. In a typical procedure, L-PheAD (70 mg, 0.088 mmol) was dissolved in n-propanol (2.1 g) with gentle heating until complete dissolution occurred. Subsequently, TIP (175 mg, purchased from Aladdin) was added to the solvent with stirring at room temperature for 10 min. The mixture was allowed to react at 0 °C with stirring for 2 h. Transferring these mixtures into the constant temperature humidity incubator and the sample was dried at 25 °C and 60% RH for 5 days, then vacuum dried at 50 °C for 24 h to completely remove the solvent, which resulted in a light purple powder. All organics in this product were removed by calcination at 600 °C, and chiral imprinted TiO₂ (TiO₂-2l) was obtained.

Preparation of TiO₂-based organic-inorganic nanoheterojunctions. Dissolve 1 mg L/D-PheAD in 1 mL acetonitrile.

Meanwhile, 1 mg TiO₂ was dispersed in 1 mL water. 100 μl of L-PheAD solution and 0–50 μl of TiO₂ dispersion were added to different ratios of water and acetonitrile mixture, and then sonicated for 30 min, finally the TiO₂-based organic-inorganic nanoheterojunctions were obtained by evaporating the solvent.

Measurement of band gap

Electrochemical gaps. The determination of electrochemical gaps was conducted using a CHI660E electrochemistry workstation manufactured by Shanghai Chenhua Instruments Co., China. Cyclic voltammetry (CV) experiments were performed in a dehydrated and deoxygenated dichloromethane solution with 0.1 M Bu₄NPF₆ serving as the supporting electrolyte. For the electrochemical experiments, a platinum foil measuring 1 × 5 mm was employed as the auxiliary electrode, and an Ag/AgCl electrode was used as the reference electrode. The working electrode consisted of a solution (10 μL) containing TiO₂-2l/L-PheAD/TiLL-7, drop-cast onto a glassy carbon electrode (GCE) with a diameter of 5 mm. The CV scan potential sweep range extended from –1.6 V to 1.6 V, with a scanning speed of 50 mV/s. The onset potentials of the oxidation and reduction waves, denoted as E_{ox,onset} and E_{red,onset}, respectively, were determined. To ensure accuracy, all cyclic voltammograms were meticulously calibrated against the Fc/Fc⁺ redox couple in the respective solvents. The electrochemical band gap was calculated from oxidation and reduction potentials, and the calculation formula for the electrochemical gaps is as follows:

$$E_{\text{HOMO}}^{\text{elec}} = -(E_{\text{ox,onset}} + 4.8) \text{ eV}; E_{\text{LUMO}}^{\text{elec}} = -(E_{\text{red,onset}} + 4.8) \text{ eV}$$

Optical gaps. We harnessed the Kubelka–Munk function within the spectrum of diffuse reflectance. To correlate photon energy ($h\nu$) with the absorption coefficient (A) in semiconductor materials, we employed the equation^{35,36}:

$$(Ah\nu/K)^n = h\nu - E_g$$

K represents the absorption constant for direct transitions, A signifies the diffuse reflectance UV absorbance, $h\nu = 1240/\lambda$, and n is an index dependent on the nature of the electronic transition responsible for absorption. For direct band gap $n = 1/2$ and indirect band gap $n = 2$ ³⁷. In the context of organic semiconductors, n is generally assumed to be $1/2$ ³⁸.

Measurement of charge transfer performance

Conductive AFM. Conductive AFM measurements were conducted on TiO₂, L-PheAD, and TiO₂-based organic-inorganic nanoheterojunctions. These materials were drop-cast on silicon wafer, following a described test method found in the literature⁶². The measurement of transport properties in this configuration involves using a metallic AFM tip as the top electrode contact to the apex of a nanoparticle, while the silicon substrate acts as the bottom electrode.

Electrochemical impedance spectroscopy (EIS). Employing a platinum foil (1 × 5 mm) as the auxiliary electrode and a saturated calomel electrode (SCE) as the reference electrode. We assessed the prepared catalysts/GCE as the working electrode (comprising a 10 μL solution containing TiO₂-2l/L-PheAD/TiLL-7, drop-cast onto a GCE with a 5 mm diameter), and utilized the copper wire as a conductor. The EIS measurement was carried out in a 5.0 mM K₃Fe(CN)₆ - K₄Fe(CN)₆ and 0.1 M KCl solution at open potential.

Photoresponse test. To assess the photoresponse of TiO₂, L-PheAD, and TiO₂-based organic-inorganic nanoheterojunctions, we used the PLS-SXE300/300 UV xenon lamp system. This test

involved applying a set of long-pass filters, with bias voltages set at -0.65 V under 365 nm and 400–780 nm radiation.

Mott-Schottky (M-S) measurement. We employed a three-electrode configuration with the TiO_2 , L-PheAD, and TiO_2 -based organic-inorganic nanoheterojunctions/GCE as the working electrode. The reference electrode was a SCE, and the counter electrode was platinum. The measurement was conducted using a 0.2 M KCl electrolyte, and notably, all measurements were conducted in dark conditions.

Structural characterization

Circular dichroism (CD) spectra. We examined the CD and dynamic CD spectra of TiO_2 , L-PheAD, and TiO_2 -based organic-inorganic nanoheterojunctions. This investigation took place in the UV region spanning a range of 190 to 400 nm. We carried out these measurements within a 0.1 mm quartz cuvette, maintaining a concentration of 1 mg/mL with a JASCO J-1500 spectrometer. **Diffuse reflectance ultraviolet-visible-near-infrared (UV-Vis-NIR) spectroscopy:** Diffused reflectance (DR) measurements was employed to determine the UV-Vis-NIR spectrophotometer with Lambda 950, spanning a wavelength range from 200 to 900 nm. This system was designed by using the integrating sphere attachment with BaSO_4 as a reference material. **Fluorescence emission spectra:** We meticulously recorded fluorescence spectra in both steady-state and time-resolved modes, employing a fluorescence spectrofluorometer (QM/TM/IM). **Fourier transform infrared (FTIR) spectra:** FTIR spectra were meticulously obtained using a Shimadzu FT-IR Instrument. For solid-state measurements, the KBr disk technique was selected. **Scanning electron microscopy (SEM):** SEM images were captured using the Sirion 200 & INCA X-Act Microscope. Sample preparation involved depositing diluted suspensions (at a concentration of 1 mg/mL) onto silicon wafers. After drying, a thin layer of Au was applied to enhance contrast and clarity. **Transmission electron microscopic (TEM) and selected area electron diffraction (SAED):** We studied TiO_2 , L-PheAD, and TiO_2 -based organic-inorganic nanoheterojunctions using the Talos F200X G2 TEM. The samples for TEM and SAED analysis were prepared by depositing drops of respective suspensions onto copper grids, followed by ambient drying. Multiple crystals were analyzed for each sample to ensure accuracy and reproducibility. **X-ray diffraction (XRD):** Powder XRD analysis was conducted using D8 Advance (Bruker) with Cu K α radiation. **X-ray photoelectron spectroscopy (XPS):** The XPS analysis was accomplished using AXIS Ultra DLD photoelectron spectrometer (Kratos Analytical). **NMR spectra:** Detailed insights into the structural composition were acquired through NMR spectra with a Bruker AVANCE III HD 500 Instrument (500 MHz) spectrometer. We recorded these spectra with partially deuterated solvents as internal standards. Coupling constants (J) were expressed in Hz and chemical shifts (δ) in ppm, and multiplicities categorized as s (singlet), d (doublet), t (triplet), m (multiplet).

Photocatalytic performance test

Photocatalytic H_2 evolution measurements. Photocatalytic hydrogen production was carried out in a top-irradiation Pyrex reaction vessel connected to a closed glass gas system. Typically, 10 mg photocatalyst powder was dispersed in 20 ml aqueous with 10 mg ascorbic acid and then illuminated with a 300 W Xe lamp (PLS-SXE300/300UV, Trusttech Co., Ltd). The temperature of reaction solution was maintained at 0 °C in an ice bath. The produced hydrogen was analyzed using an online gas chromatography (Nexis GC-2030, 5 Å molecular sieve column, and N_2 as carrier gas).

Photodegradation of organic pollutants. Photodegradation of organic pollutants was conducted in an opening quartz chamber (10 mL) vertically irradiated by a 300 W high-pressure Xe lamp located on the upper position. The light density was controlled at 1000 mW cm^{-2} . The irradiation area was ca. 7 cm^2 . Reaction conditions: temperature, 0 °C; C_0 (RhB) = 450 $\mu\text{mol L}^{-1}$; C_0 (MV) = 1500 $\mu\text{mol L}^{-1}$ and catalyst: 0.5 g L^{-1} (TiO_2 -2l or L-PheAD or TiLL-7); no acid or alkaline reagents.

Incident photo-to-current efficiency (IPCE). The IPCE was calculated according to the following equation:

$$\text{IPCE} = \frac{1240 \times J_{\text{ph}}}{\lambda \times I_{\text{light}}} \times 100\%$$

Where J_{ph} is the photocurrent density ($\mu\text{A cm}^{-2}$), λ is the incident light wavelength (nm), and I_{light} is the incident light power ($\mu\text{W cm}^{-2}$) for each wavelength.

Data availability

The main data supporting the findings of this study are available within the paper and its Supplementary Information. Additional data are available from the corresponding authors upon reasonable request.

Received: 22 May 2023; Accepted: 17 October 2023;

Published online: 30 October 2023

References

- Son, H.-J., Pac, C. & Kang, S. O. Inorganometallic photocatalyst for CO_2 reduction. *Acc. Chem. Res.* **54**, 4530–4544 (2021).
- Gu, J. et al. Water reduction by a p-GaInP $_2$ photoelectrode stabilized by an amorphous TiO_2 coating and a molecular cobalt catalyst. *Nat. Mater.* **15**, 456–460 (2016).
- Ma, Y. et al. Selective photocatalytic CO_2 reduction in aerobic environment by microporous Pd-porphyrin-based polymers coated hollow TiO_2 . *Nat. Commun.* **13**, 1400 (2022).
- Jiang, Z. et al. Filling metal-organic framework mesopores with TiO_2 for CO_2 photoreduction. *Nature* **586**, 549–554 (2020).
- Wang, S. et al. Porous hypercrosslinked polymer- TiO_2 -graphene composite photocatalysts for visible-light-driven CO_2 conversion. *Nat. Commun.* **10**, 676 (2019).
- Xie, Q. et al. Nanosheet-based titania microspheres with hollow core-shell structure encapsulating horseradish peroxidase for a mediator-free biosensor. *Biomaterials* **32**, 6588–6594 (2011).
- Zhang, H., Ono, L. K., Tong, G., Liu, Y. & Qi, Y. Long-life lithium-sulfur batteries with high areal capacity based on coaxial CNTs@TiN- TiO_2 sponge. *Nat. Commun.* **12**, 4738 (2021).
- Sun, X. et al. Shape-stabilized composite phase change material PEG@ TiO_2 through in situ encapsulation of PEG into 3D nanoporous TiO_2 for thermal energy storage. *Renew. Energy* **170**, 27–37 (2021).
- Kumar, A., Khan, M., He, J. & Lo, I. M. C. Recent developments and challenges in practical application of visible-light-driven TiO_2 -based heterojunctions for PPCP degradation: a critical review. *Water Res.* **170**, 115356 (2020).
- Acharya, R. & Parida, K. A review on $\text{TiO}_2/\text{g-C}_3\text{N}_4$ visible-light-responsive photocatalysts for sustainable energy generation and environmental remediation. *J. Environ. Chem. Eng.* **8**, 103896 (2020).
- Li, C.-C. et al. Rational combination of covalent-organic framework and nano TiO_2 by covalent bonds to realize dramatically enhanced photocatalytic activity. *Appl. Catal. B: Environ.* **266**, 118586 (2020).
- Zhong, Y.-H. et al. Design of an alkaline pyridyl acceptor-based calix[4]arene dye and synthesis of stable calixarene- TiO_2 porous hybrid materials for efficient photocatalysis. *J. Mater. Chem. A* **8**, 8883–8891 (2020).
- Zhang, X. et al. 3D TiO_2 @nitrogen-doped carbon/Fe $_7$ S $_8$ composite derived from polypyrrole-encapsulated alkalized MXene as anode material for high-performance lithium-ion batteries. *Chem. Eng. J.* **385**, 123394 (2020).
- Li, R. et al. Well-designed MXene-derived Carbon-doped TiO_2 coupled porous g- C_3N_4 to enhance the degradation of ciprofloxacin hydrochloride under visible light irradiation. *Sep. Purif. Technol.* **295**, 121254 (2022).

15. Tobaldi, D. M. et al. Graphene-TiO₂ hybrids for photocatalytic aided removal of VOCs and nitrogen oxides from outdoor environment. *Chem. Eng. J.* **405**, 126651 (2021).
16. Maleki, A. Green oxidation protocol: Selective conversions of alcohols and alkenes to aldehydes, ketones and epoxides by using a new multiwall carbon nanotube-based hybrid nanocatalyst via ultrasound irradiation. *Ultrason. Sonochem.* **40**, 460–464 (2018).
17. Deng, B. et al. Sandwich-like Fe₃O₄@TiO₂/C nanocomposites derived from MXene/Fe-MOFs hybrids for electromagnetic absorption. *Nano-Micro Lett.* **12**, 55 (2020).
18. Liu, D. et al. Porous BN/TiO₂ hybrid nanosheets as highly efficient visible-light-driven photocatalysts. *Appl. Catal. B: Environ.* **207**, 72–78 (2017).
19. Yu, G., Jie, K. & Huang, F. Supramolecular amphiphiles based on host-guest molecular recognition motifs. *Chem. Rev.* **115**, 7240–7303 (2015).
20. Yang, X., Yuan, D., Hou, J., Sedgwick, A. C. & Wang, L. Organic/inorganic supramolecular nano-systems based on host/guest interactions. *Coord. Chem. Rev.* **428**, 213609 (2021).
21. Mo, S. et al. Tunable mechanoresponsive self-assembly of an amide-linked dyad with dual sensitivity of photochromism and mechanochromism. *Adv. Funct. Mater.* **27**, 1701210 (2017).
22. Zhang, R., Fu, Q., Zhou, K., Yao, Y. & Zhu, X. Ultra stretchable, tough and self-healable poly(acrylic acid) hydrogels cross-linked by self-enhanced high-density hydrogen bonds. *Polymer* **199**, 122603 (2020).
23. Li, L. et al. Highly efficient CdS quantum dot-sensitized solar cells based on a modified polysulfide electrolyte. *J. Am. Chem. Soc.* **133**, 8458–8460 (2011).
24. Harb, S. V. et al. A comparative study on PMMA-TiO₂ and PMMA-ZrO₂ protective coatings. *Prog. Org. Coat.* **140**, 105477 (2020).
25. Rivalta, I., Brudvig, G. W. & Batista, V. S. Oxomanganese complexes for natural and artificial photosynthesis. *Curr. Opin. Chem. Biol.* **16**, 11–18 (2012).
26. Siviero, F. et al. Hybrid n-TiO₂-CuPc gas sensors sensitive to reducing species, synthesized by cluster and supersonic beam deposition. *Sens. Actuators B: Chem.* **126**, 214–220 (2007).
27. Yang, Z. et al. Hybrid anatase/rutile nanodots-embedded covalent organic frameworks with complementary polysulfide adsorption for high-performance lithium-sulfur batteries. *ACS Cent. Sci.* **5**, 1876–1883 (2019).
28. Ke, T., Shen, S., Rajavel, K., Yang, K. & Lin, D. In situ growth of TiO₂ nanoparticles on nitrogen-doped Ti₃C₂ with isopropyl amine toward enhanced photocatalytic activity. *J. Hazard. Mater.* **402**, 124066 (2021).
29. Huang, J.-F. et al. Facile synthesis of porous hybrid materials based on Calix-3 dye and TiO₂ for high photocatalytic water splitting performance with excellent stability. *J. Mater. Chem. A* **7**, 2993–2999 (2019).
30. Karthik, P. et al. A visible-light active catechol-metal oxide carbonaceous polymeric material for enhanced photocatalytic activity. *J. Mater. Chem. A* **5**, 384–396 (2017).
31. Yano, S., Iwata, K. & Kurita, K. Physical properties and structure of organic-inorganic hybrid materials produced by sol-gel process. *Mater. Sci. Eng.: C* **6**, 75–90 (1998).
32. Kazuki, N. Sol-gel process of oxides accompanied by phase separation. *Bull. Chem. Soc. Jpn.* **79**, 673–691 (2006).
33. Huang, H., Li, Y.-X., Jiang, G.-J., Wang, H.-L. & Jiang, W.-F. In situ construction of dye-sensitized BiOCl/rutile-TiO₂ nanorod heterojunctions with highly enhanced photocatalytic activity for treating persistent organic pollutants. *Inorg. Chem.* **60**, 17325–17338 (2021).
34. Kim, H. J., Lee, M. H., Muthiac, L., Vicens, J. & Kim, J. S. Host-guest sensing by calixarenes on the surfaces. *Chem. Rev.* **41**, 1173–1190 (2012).
35. Liu, S., Yu, J. & Mann, S. Spontaneous construction of photoactive hollow TiO₂ microspheres and chains. *Nanotechnology* **20**, 325606 (2009).
36. Zhai, H. et al. Self-assembled organic-inorganic hybrid elastic crystal via biomimetic mineralization. *Adv. Mater.* **22**, 3729–3734 (2010).
37. Cölfen, H. & Mann, S. Higher-order organization by mesoscale self-assembly and transformation of hybrid nanostructures. *Angew. Chem. Int. Ed.* **42**, 2350–2365 (2003).
38. Chen, C., Loe, F., Blocki, A., Peng, Y. & Raghunath, M. Applying macromolecular crowding to enhance extracellular matrix deposition and its remodeling in vitro for tissue engineering and cell-based therapies. *Adv. Drug Deliv. Rev.* **63**, 277–290 (2011).
39. Zhu, L. et al. Controlling ultra-large optical asymmetry in amorphous molecular aggregations. *Angew. Chem. Int. Ed.* **60**, 3672–3678 (2021).
40. Liu, G., Liu, J., Feng, C. & Zhao, Y. Unexpected right-handed helical nanostructures co-assembled from l-phenylalanine derivatives and achiral bipyridines. *Chem. Sci.* **8**, 1769–1775 (2017).
41. Wen, Y., He, M.-Q., Yu, Y.-L. & Wang, J.-H. Biomolecule-mediated chiral nanostructures: a review of chiral mechanism and application. *Adv. Colloid Interface Sci.* **289**, 102376 (2021).
42. Gao, X. et al. Distinct excitonic circular dichroism between wurtzite and zincblende CdSe nanoplatelets. *Nano Lett.* **18**, 6665–6671 (2018).
43. Huang, J. & Feng, C. Aniline dimers serving as stable and efficient transfer units for intermolecular charge-carrier transmission. *iScience* **26**, 105762 (2023).
44. Wang, F. et al. Interaction mechanisms of antibiotic sulfamethoxazole with various graphene-based materials and multiwall carbon nanotubes and the effect of humic acid in water. *Carbon* **114**, 671–678 (2017).
45. Zhu, D. & Pignatello, J. J. Characterization of aromatic compound sorptive interactions with black carbon (charcoal) assisted by graphite as a model. *Environ. Sci. Technol.* **39**, 2033–2041 (2005).
46. Feng, N. et al. Efficient and selective photocatalytic CH₄ conversion to CH₃OH with O₂ by controlling overoxidation on TiO₂. *Nat. Commun.* **12**, 4652 (2021).
47. Sutiono, H. et al. Facile synthesis of [101]-oriented rutile TiO₂ nanorod array on FTO substrate with a tunable anatase-rutile heterojunction for efficient solar water splitting. *ACS Sustain. Chem. Eng.* **4**, 5963–5971 (2016).
48. Shiraiishi, Y. Resorcinol-formaldehyde resins as metal-free semiconductor photocatalysts for solar-to-hydrogen peroxide energy conversion. *Nat. Mater.* **18**, 985–993 (2019).
49. McQuade, D. T., McKay, S. L., Powell, D. R. & Gellman, S. H. Indifference to hydrogen bonding in a family of secondary amides. *J. Am. Chem. Soc.* **119**, 8528–8532 (1997).
50. Buriankova, L. et al. Synchrotron based Fourier-transform infrared microspectroscopy as sensitive technique for the detection of early apoptosis in U-87 MG cells. *Laser Phys. Lett.* **7**, 613–620 (2010).
51. Zhang, W. et al. Formation of n-n type heterojunction-based tin organic-inorganic hybrid perovskite composites and their functions in the photocatalytic field. *Phys. Chem. Chem. Phys.* **2**, 698–6989 (2018).
52. Wei, Z.-Q. et al. Polymer-mediated electron tunneling towards solar water oxidation. *Adv. Funct. Mater.* **32**, 2106338 (2022).
53. Shin, H. O. et al. Surface state-mediated charge transfer of Cs₂SnI₆ and its application in dye-sensitized solar cells. *Adv. Energy Mater.* **9**, 1803243 (2019).
54. Wang, S. et al. Titanium-defected undoped anatase TiO₂ with p-type conductivity, room-temperature ferromagnetism, and remarkable photocatalytic performance. *J. Am. Chem. Soc.* **137**, 2975–2983 (2015).
55. Preethi, L. K. et al. Nitrogen doped anatase-rutile heterostructured nanotubes for enhanced photocatalytic hydrogen production: Promising structure for sustainable fuel production. *Int. J. Hydrog. Energy* **41**, 5865–5877 (2016).
56. Sun, K. et al. Incorporating transition-metal phosphides into metal-organic frameworks for enhanced photocatalysis. *Angew. Chem. Int. Ed.* **59**, 22749–22755 (2020).
57. Sarkar, S. et al. Giant increase in the metal-enhanced fluorescence of organic molecules in nanoporous alumina templates and large molecule-specific red/blue-shift of the fluorescence peak. *Nano Lett.* **14**, 5973–5978 (2014).
58. Kang, T., Wang, H., Wang, X. & Feng, L. A facile Zn(II) probe based on intramolecular charge transfer with fluorescence red-shift. *Microchem. J.* **148**, 442–448 (2019).
59. Bel Haj Mohamed, N. et al. Time resolved and temperature dependence of the radiative properties of thiol-capped CdS nanoparticles films. *J. Nanopart. Res.* **16**, 2242 (2014).
60. Zhang, F., Li, X., Zhao, Q., Chen, G. & Zhang, Q. High-performance In₂O₃@PANI core@shell architectures with ultralong charge carriers lifetime for photocatalytic degradation of gaseous 1,2-dichlorobenzene. *Appl. Catal. B: Environ.* **263**, 118278 (2020).
61. Na, C. W. et al. Photoluminescence of Cd_{1-x}Mn_xS (x ≤ 0.3) nanowires. *J. Phys. Chem. B* **110**, 6699–6704 (2006).
62. Wang, Y. et al. Graphene-assisted solution growth of vertically oriented organic semiconducting single crystals. *ACS Nano* **9**, 9486–9496 (2015).

Acknowledgements

The authors gratefully acknowledge the financial support for this research from the National Nature Science Foundation of China (NSFC 51833006), Scientific Research Program of the Higher Education Institution of Xinjiang (XJEDU2017S048), Leading Talents in Science and Technology Innovation under the National Ten Thousand Talents Plan, SJTU Trans-med Awards Research (No.WF5401X62X603), Science and Technology Commission of Shanghai Municipality (20S31904600).

Author contributions

C.F. supervised this project. J.H. performed most of the experiments and analyzed the experimental data. J.H., J.X., and S.B. wrote and revised the manuscript. All authors discussed the results and assisted during manuscript preparation.

Competing interests

The authors declare no competing interests.

Additional information

Supplementary information The online version contains supplementary material available at <https://doi.org/10.1038/s43246-023-00415-x>.

Correspondence and requests for materials should be addressed to Chuanliang Feng.

Peer review information *Communications Materials* thanks Feng-Ming Zhang and the other, anonymous, reviewer(s) for their contribution to the peer review of this work. Primary Handling Editor: Jet-Sing Lee.

Reprints and permission information is available at <http://www.nature.com/reprints>

Publisher's note Springer Nature remains neutral with regard to jurisdictional claims in published maps and institutional affiliations.



Open Access This article is licensed under a Creative Commons Attribution 4.0 International License, which permits use, sharing, adaptation, distribution and reproduction in any medium or format, as long as you give appropriate credit to the original author(s) and the source, provide a link to the Creative Commons licence, and indicate if changes were made. The images or other third party material in this article are included in the article's Creative Commons licence, unless indicated otherwise in a credit line to the material. If material is not included in the article's Creative Commons licence and your intended use is not permitted by statutory regulation or exceeds the permitted use, you will need to obtain permission directly from the copyright holder. To view a copy of this licence, visit <http://creativecommons.org/licenses/by/4.0/>.

© The Author(s) 2023